Simultaneous Orthogonal Imaging for Cold Flow Characterization of Additively Manufactured Injector Elements

Ari D. Goldman*, Murphy Mitchell†, David E. Scarborough‡, and T. Teasley§
Auburn University, Auburn, Alabama, 36849

Additively manufactured (AM) injectors have the potential to improve characteristic velocity (C*) performance beyond the 90-97% of theoretical C* performance seen by traditionally manufactured (TM) combustion device injectors. Maximized C* performance yields high overall combustion efficiency in all types of combustion devices, particularly liquid rocket engines (LREs) and rotating detonation rocket engines (RDREs). A high degree of propellant atomization and mixedness is required to achieve maximum C* performance and therefore high overall combustion efficiency. This study focused on measuring and comparing the performance of different novel AM injector elements over a broad range of operating conditions under high pressure, cold flow. As part of this work, a high pressure, cold flow experimental spray facility was designed to measure each element's injector spray patterns under pressures ranging from 50 to 1000 psig and stiffness ratios from 0.5 to 2.0. Preliminary results are presented from orthogonal, simultaneous imaging comparing atomization and spray geometry between quad, trio, pentad, slotted, and triplet impingers in gas-liquid flow.

I. Introduction

Current liquid rocket engines (LREs) overall combustion efficiency is limited by unrealized characteristic velocity (C*) performance. LREs built with traditionally manufactured (TM) combustion device injectors are limited to 90-97% of theoretical C* performance. Next-generation, high-performance propellant injectors have the potential to achieve significantly improved C* efficiency for both LREs and rotating detonating rocket engines (RDREs). These high-performance propellant injectors incorporate novel internal and external flow structures that can only be produced using modern additive manufacturing (AM) techniques. Metal AM techniques such as laser powder bed fusion (L-PBF) and laser powder directed energy deposition (LP-DED) hold the potential to improve upon conventional machining limits. Figure 1 shows the theoretical performance improvement between optimized AM injector schemes and current traditionally manufactured injectors.

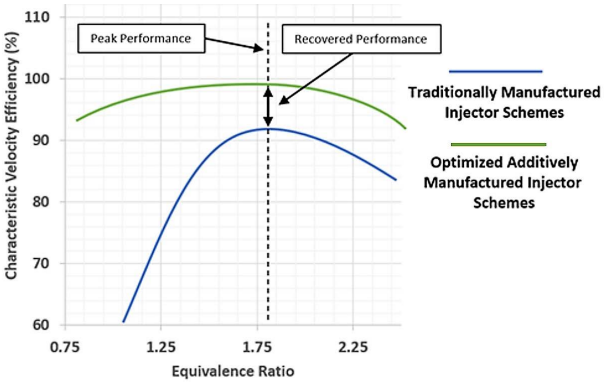

Fig. 1 Performance comparison between a traditionally manufactured injector versus an optimized additively manufactured injector with minimized losses.

Cost comparisons between AM and TM parts are difficult due to inherent differences in the manufacturing techniques. Detailed, direct per unit pricing cannot be compared however, it is generally true that AM is more cost effective than TM for low product volume and high product complexity [1]. This makes AM a suitable solution for high-performance propellant injectors. When comparing bulk production pricing between AM and TM, direct and indirect costs must be considered. For AM, direct costs are generally lower and include part geometry, feedstock, alloy composition, machine time, machine accessibility, and post-processing. Initial indirect costs are high, requiring initial machinery purchase, equipment maintenance, print setup, and power consumption [1, 2].

*Graduate Research Assistant, Aerospace Engineering, AIAA Student Member.
†Undergraduate Research Assistant, Aerospace Engineering, AIAA Student Member.
‡Associate Professor, Aerospace Engineering, AIAA Member
§NASA MSFC

Printing a more complex part may cost approximately the same amount in material as a simple part. However, studies have shown that increases in complexity cause increases in build time, failure rates, and post-processing operations which will incur greater cost[3, 4]. Added component complexity must therefore be considered in cost analysis. As a first step in determining if the performance increase from novel orifice geometries is worth the additional cost of AM, this study characterized the spray patterns resulting from quad, trio, pentad, slotted, and triplet impinger injectors, shown in 2.

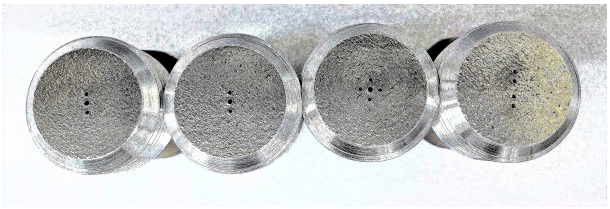

Fig. 2 Quad, trio, pentad, slotted, and triplet impinger injectors.

The two flow configurations tested were gas-liquid-gas (GLG), also referred to as liquid centered flow, and liquid-gas-liquid (LGL), also referred to as gas centered flow. Liquid centered flow had gas supply plumbed to the outer orifices and liquid supply plumbed to the inner orifice. Gas centered flow had liquid supply plumbed to the outer orifices and gas supply plumbed to the inner orifice. Both configurations are forms of gas-liquid flow, referring to the use of both gas and liquid supply. Studies have shown that gas-liquid injection may reduce recovery requirements in RDEs [5–7].

Large ΔP s in gas-liquid flows cause spray fields which move faster than most high-speed cameras can capture. To overcome this, the sprays were illuminated with a pulsed laser. To better understand the spray geometry, two cameras simultaneously photographed the spray orthogonally from the front and side. The resulting image pairs were then processed for spray spread angle. The spread angle was obtained by first identifying the spray boundary, applying a linear fit to each outer edge, and then calculating the spray spread angle between the linear fit lines.

II. Background

Gas-liquid sprays are used in an extensive range of applications such as treatments, coating, oil burners, gas turbines, and rocket fuel injection. As such, many techniques have been developed to analyze these sprays under a wide variety of condition. Sprays are commonly characterized by droplet size, velocity and distribution, spray field structures and density, as well as bulk properties like spread angle, volume and mixture ratio [8].

One commonly characterized spray parameter is effective atomization. Atomization is typically considered qualitatively through visual comparisons but is often coupled with quantitative droplet size measurements. Effective atomization can be determined through cold flow testing. To properly visualize injector atomization requires the use of high-speed photography and/or high powered, pulsed laser illumination [9–11]. Additional means of quantifying atomization include high-speed shadowgraphs, phase-doppler particle analyzers [12], and Malvern particle sizers [13]. See Teasley et al. [14] for the role efficient atomization and mixing plays in high performance combustion [14].

Effective atomization is essential for good combustion efficiency in both LREs and RDREs, though it is typically limited to a narrow range of operating conditions and fuel-oxidizer mixture ratios [15]. Suboptimal atomization and mixing has been reported to negatively impact wave speeds and limit operating frequencies [16]. The mixing time is a balance between sufficient mixing and overmixing. Overmixing can lead to parasitic deflagration, yet another source of inefficiency [17]. Numerical works with RDREs have shown increasing injector mixing can lead to performance improvements [18, 19].

Spread angle is another critical parameter frequently analyzed in cold flow spray imaging. Spray angle can be identified by calculating the angle between the left and right outer boundaries of the spray. This information is used by engineers to design injector element layout and is necessary for optimized intra-injector mixing. Spray angle is commonly compared to various other test parameters like nozzle geometry, gas to liquid density ratio, injection velocity, weber number, mass flux ratio, pressure drop across the injector, and stiffness ratio [20–22].

Local atomization and spread angle were the parameters chosen to characterize these injectors. Atomization was determined qualitatively and spread angle was determined quantitatively from instantaneous images taken simultaneously with a high powered laser. These images were then compared to better understand how different AM injectors perform across a range of stiffnesses and pressure drops across the injectors for GLG and LGL flow configurations. These injectors were then compared based on these parameters.

III. Methodology

Propellant injectors are often subject to a wide range of operating conditions and flow disturbances that can greatly affect their atomization and mixing characteristics. Therefore, experiments were conducted on five injectors at stiffnesses of 0.5, 1.0, and 2.0 and liquid side supply pressures of 150, 250, 500 psig. These stiffnesses were chosen to represent reasonable engine operating conditions. For water pressures below 150 psig, the desired spray field did not form due lack of sufficient gas impingement to cause stream breakup. Therefore, experiments were limited to pressures above 150 psig. The gas supply pressure determined by stiffness ratio and liquid supply pressure can be found below in Table 1. The experimental facility was limited to a maximum pressure of 1,000 psig. Tests which would require gas supply pressures exceeding the maximum pressure limit were excluded from the experimental matrix for safety concerns. Stiffness ratios were calculated from Equation 1. Here ΔP refers to the pressure difference between the injector supply pressure and the chamber pressure (P_c). Chamber pressure was atmospheric for this experiment.

Table 1 Gas supply pressure based on stiffness and water supply pressure

Stiffness	Liquid Supply Pressure (psig)		
	150	250	500
0.5	75	125	250
1.0	150	250	500
2.0	300	500	1000

$$\text{Stiffness Ratio} = \frac{\Delta P_{\text{gas}} / P_c}{\Delta P_{\text{liquid}} / P_c} \tag{1}$$

A. Experimental Facility

A high pressure, cold flow, optically accessible spray facility, see Figure 3, was developed to safely conduct this study. Water and nitrogen were chosen as surrogates for oxidizer and fuel. The facility consisted of two pressurizing flow paths for the liquid and gas supply to the injector elements. Both paths began with a high-pressure nitrogen gas cylinder and regulators which enabled pressure control. The gas supply line split immediately downstream of the regulator to allow for a relief line controlled with a needle valve. The main gas line continued into a safety relief valve, a solenoid, and an additional needle valve for flow control. Downstream of this needle valve was a nitrogen flow meter coupled with a pressure gauge immediately upstream of the gas port of the injector element. The gas supply system delivered nitrogen at pressures ranging from 50-1000 psig to the injector element.

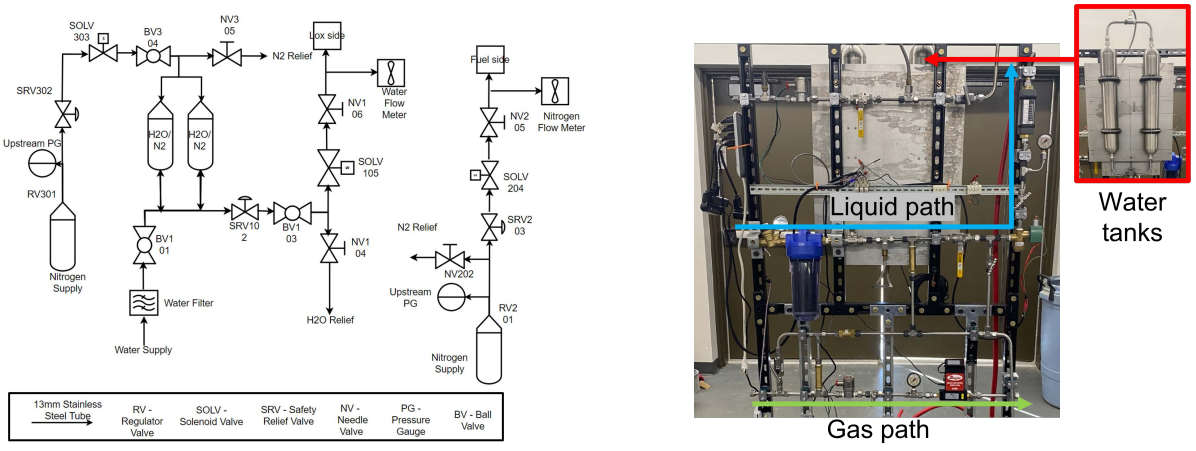

(a) **(b)**

Fig. 3 Engineering schematic (a) and flow paths (b) of the optically accessible, high pressure, cold flow spray experiment.

Downstream of the liquid supply path regulator was a safety relief valve for relieving any nitrogen overpressuring. The nitrogen flow path then splits to allow for a relief line controlled with a needle valve. The main line led into water tanks safety rated over 1000 psig. These tanks were filled via a separate water fill line consisting of a hose inlet, a water filter, and a ball valve for control. Downstream of the water tanks, the main liquid line was fitted with a safety relief

valve and a ball valve for control. This line then branched off into a liquid relief line controlled by a needle valve. The main liquid line continued into a solenoid valve and a needle valve for flow control. Just upstream of the liquid port of the injector was a flow meter coupled with a pressure gauge. The liquid supply system can deliver water at pressures ranging from 50-1000 psig at flow rates ranging from 0.2-2.0 GPM. The nozzle spray discharged at atmospheric pressure where the spray field was captured by the imaging system. The five injectors studied were quad, trio, pentad, slotted, and triplet impinger injectors, which were additively manufactured using L-PBF.

B. Imaging Systems and Image Processing

Two Lucid Vision Labs Phoenix 8.9 MP monochrome cameras were used to acquire simultaneous orthogonal images of the nozzle spray. Each camera was outfitted with an IRIX 150mm macro 1:1 lens allowing for a focus volume of 55 mm by 35 mm by 11 mm directly below the nozzle face. The smallest in-focus, resolvable droplet diameter was 133.31 μm (Table 2). Droplets at or below this diameter are considered very fine, as classified by the American Society for Agricultural and Biological Engineers (ASABE) standard [23]. The cameras were positioned 90 degrees from each other to obtain front and side views of the spray. For the injectors which produced a non-symmetric spray, the wider spray spread angle was viewed by camera 1 (Fig. 4).

Table 2 Imaging system parameters

Experimental Characteristics		
Focal Length (mm)	150	
Aperture	f/32	
Distance to Object (ft)	2.5	
Depth of Field (mm)	10.60	
Camera Characteristics	Horizontal	Vertical
Sensor Size (px)	4096	2160
Pixel Size (mm)	3.45	3.45
Image Space Resolution (μm)	144.93	144.93
Sensor Dimensions (mm)	14.13	7.45
Lens Characteristics	Horizontal	Vertical
Field of View (mm)	53	35.30
Primary Magnification	0.27	0.21
Resolvable Droplet Diameter (μm)	133.31	105.55

Simultaneous, orthogonal imaging allowed for capture of the spray from multiple views. Short pulse illumination was required to prevent object blurring. Object blurring occurs when the image of an object travels greater than one-pixel on the sensor within the span of the sensor's exposure to illumination. To prevent this from occurring, illumination was provided via a dual-pulse Nd:YAG laser (New Wave Solo III, 50 mJ/pulse) with a 20 ns pulse duration. A neutral density (ND) filter was placed in the beam path to minimize overexposure of the camera sensors. For tests with liquid side supply pressures of 150 and 250 psig, an ND filter with an optical density of 0.2 was used. For tests with liquid side supply pressures of 500 psig, an ND filter with an optical density of 0.4 was used. After the ND filters, a plano-convex 150 mm lens was used to expand the beam to illuminate the focus volume. Laser pulses were synchronized with the start of each frame acquisition via a programmable timing unit. The entire system was controlled through LabVIEW.

Spray angle was then determined for each image via the process seen in Table 3. In each test 20 spray image sets were taken at a rate of 2 Hz for a test duration of 10 seconds. The spray boundary identification process proceeds as follows. The spray images were converted to binary using Otsu's method for binarization [24]. The voids within the spray were filled using morphological dilation with a diamond shaped structure element [25]. The image was divided into rows and the boundaries were identified as the first and last pixel of each row to contain a non-zero value. Linear fit was set to intercept with the initial outer edges of the spray on the left and right sides and fit to the left and right boundaries. Least-squares regression was used for this linear fit.

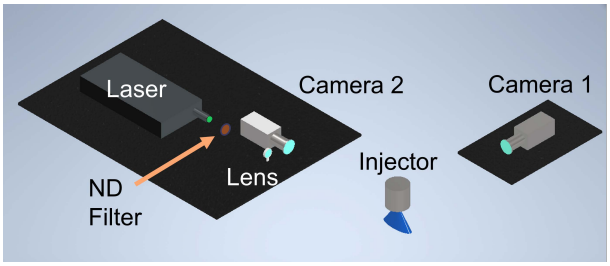

Fig. 4 Diagram of the spray imaging system.

Spread angle of the spray was then calculated using Equation 2, where state 1 represents the left border of the spray and state 2 represents the right border of the spray. Variables m_1 and m_2 are the slopes of the two lines and α represents the spray angle between the two boundaries.

$$
\begin{aligned}
y_1 &= m_1 x + b_1 \\
y_2 &= m_2 x + b_2 \\
\alpha &= \tan^{-1}\left(\frac{m_2 - m_1}{1 + m_1 m_2}\right)
\end{aligned}
\tag{2}
$$

Spray angle identification was done for each image taken for each condition. The average and standard deviation of each condition was then calculated and plotted as functions of liquid side supply pressure and stiffness. This process was repeated for each configuration.

Table 3 Spray angle processing

(a) Original Image: Pentad, GLG, Stiff 1.0, Pressure 500 psig

(b) Step 1: Binarization of the image.

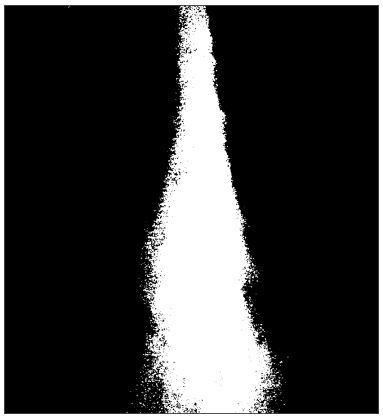

(c) Step 2: Fill to unification.

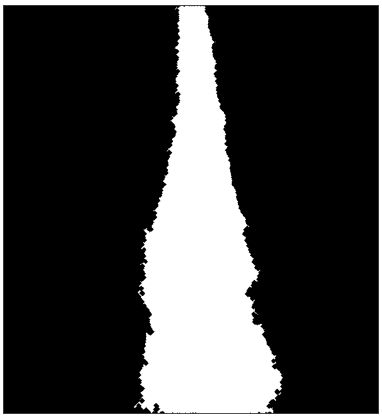

(d) Step 3: Boundary identification

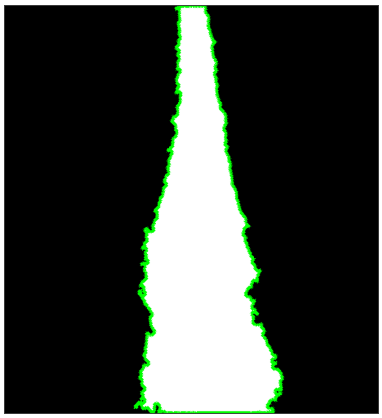

(e) Step 4: Least-squares regression for pinned linear fit.

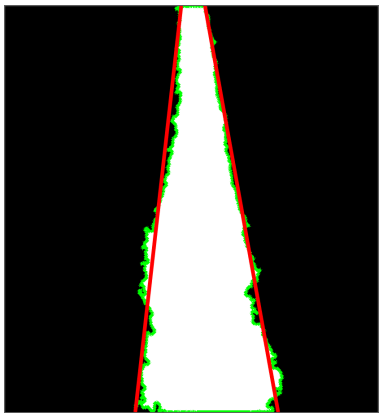

(f) Final product – Spray angle of 16.69 degrees

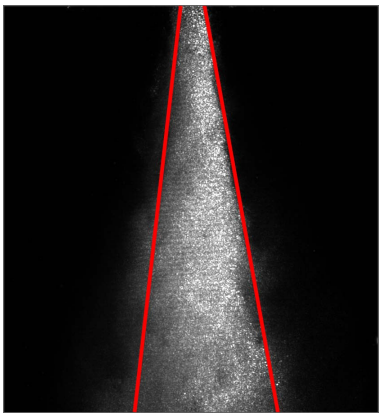

IV. Results and Discussion

This section presents experimental, instantaneous spray measurements for additively manufactured quad, trio, pentad, slotted, and triplet impinger injectors. These injectors were cold flow tested under a range of stiffnesses from 0.5–2.0 and liquid pressure drops from 150-500 psi in liquid centered and gas centered configurations. These images were analyzed to obtain both quantitative and qualitative information about the spray including local regions of atomization,

larger droplet regions and spread angles from both camera views.

In this study the minimum resolvable droplet diameter was 133 μm, representing a very fine spray as defined by ASABE [23]. Areas where droplet sizes were below the resolvable diameter appear hazy or indistinct. These areas are considered regions of atomization as seen circled in blue in Figure 5. Regions of the spray where droplets are resolvable are also identified. These areas are referred to as large droplet regions as seen circled in green in Figure 5. Changes in these regions due to increases in ΔP and stiffness are addressed.

Injector spray field spread angles determined from both camera views are plotted against stiffness and liquid side ΔP to assess dependence. Error bars representing one standard deviation are included for each point plotted. These results are still preliminary, and the trends seen in these plots do not necessarily reflect repeatable behavior for injectors beyond the ones investigated in this study.

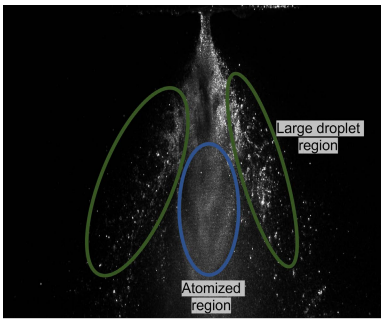

Fig. 5 Analyzed regions of a spray field.

A. Liquid Centered Configuration

The first configuration explored was the liquid centered. In this configuration, the outer orifices were plumbed with gas, and the inner, liquid, as shown in Figure 6. Figure 7 shows instantaneous spray images for a range of stiffnesses from camera view 1 while maintaining a constant liquid side ΔP of 250 psi. Figure 8 shows instantaneous spray images for a range of liquid side ΔP from camera view 1 while maintaining a constant stiffness of 1.0. The bottom rows of these figures display spray angle as a function of stiffness and liquid side ΔP, respectively. Spray angle was determined for each image via the process seen in Table 3. In each test 20 spray image sets were taken at a rate of 2 Hz for a test duration of 10 seconds. The average spray angle and standard deviation were then calculated. Spray angles from both cameras are shown with error bars representing one standard deviation. Every column represents a different injector. Reference scaling is included for visual comparison.

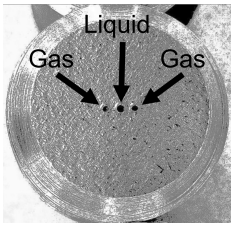

Fig. 6 Orifice identification of a liquid centered configuration.

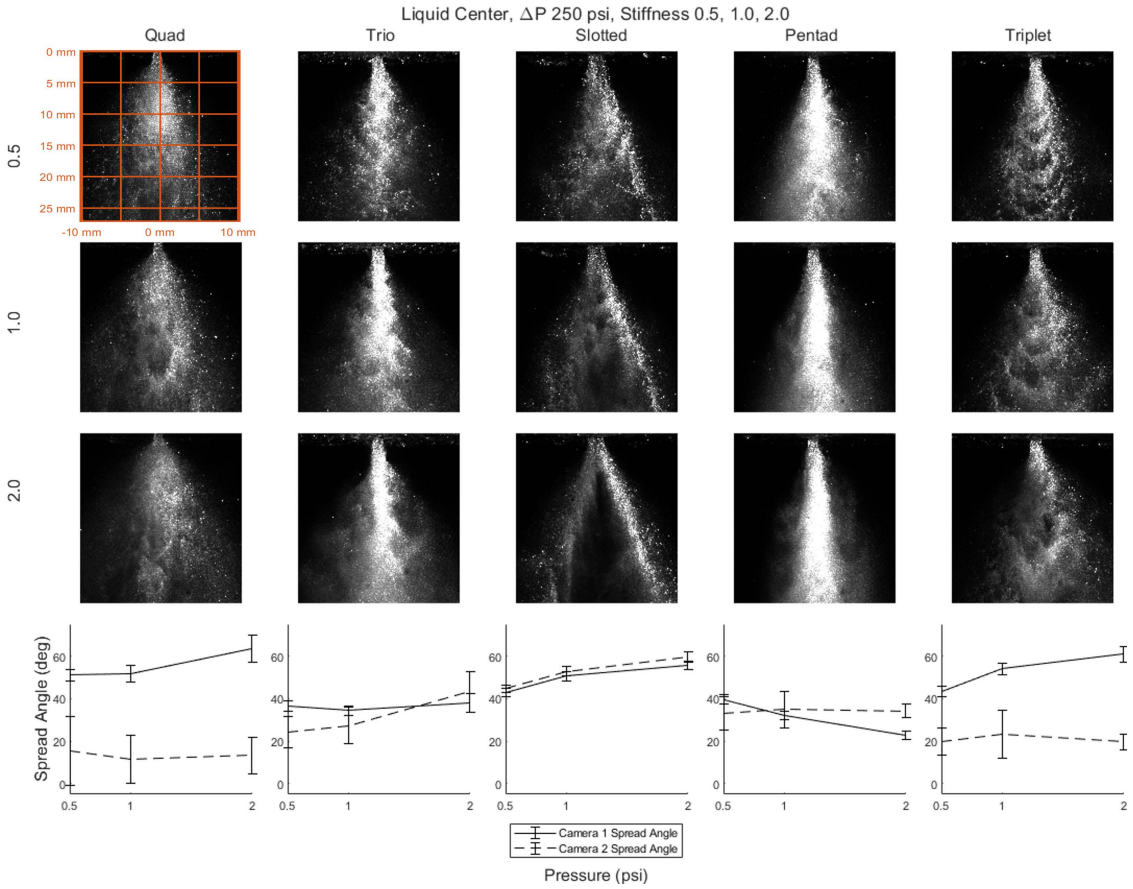

Fig. 7 Instantaneous injector spray images, varying in stiffness, for constant liquid side ΔP of 250 psi, in liquid centered configuration.

For the quad injector, the atomized region was located primarily in the center of the spray, beginning approximately 5 mm from the face of the injector. The size and location of this region remained approximately constant as stiffness was increased. At all stiffnesses, the large droplets were ejected to the edges of the spray. Fewer large droplets were seen as stiffness was increased. Camera 1 spread angle increased slightly as stiffness was increased, while camera 2 spread angle remained relatively constant as stiffness was increased. Camera 2 spread angle was significantly smaller than camera 1 spread angle at each stiffness, suggesting the spray was non-symmetric, and more fan-like in nature.

Analysis of the trio injector is limited due to overexposure seen in the upper region and center of the spray field. Only regions of adequate exposure are considered in this analysis. Atomization at a stiffness of 0.5 was confined to a small region approximately 15 mm from the face of the injector. As stiffness increased, this atomized region grew, consuming the entirety of the spray at a stiffness of 2.0. At a stiffness of 0.5 a majority of the spray consisted of large droplets. At a stiffness of 1.0, few large droplets were seen around the outer boundary of the spray and at a stiffness of 2.0, no large droplets could be found. Camera 1 spread angle remained relatively constant as stiffness was increased, while camera 2 spread angle increased slightly as stiffness was increased. Camera 1 and camera 2 spread angles were approximately the same at each stiffness, suggesting greater symmetry in the spray field.

For the slotted injector, at a stiffness of 0.5, atomization was limited to a small region approximately 25 mm from the face of the injector. At a stiffness of 1.0, a region of atomization was found between 10 and 20 mm from the face of the injector. No region of atomization was found at a stiffness of 2.0. At a stiffness of 0.5, the entire spray field outside of the small region of atomization consisted of large droplets. At stiffnesses of 1.0 and 2.0, the large droplet regions were limited to the boundary of the spray field. At a stiffness of 2.0, no spray droplets of any kind were found in the center of

the spray. Spread angles from both camera views were very similar at every stiffness, increasing slightly as stiffness increased. Despite this, the lack of droplets found in the center of the spray suggests this spray field was not symmetric.

Analysis of the pentad injector is limited due to overexposure seen in the upper region and center of the spray field. Only regions of adequate exposure are considered in this analysis. Atomization was seen throughout the spray, excluding the overexposed region, at all three stiffnesses. Occasional large droplets were seen in the outer regions of the spray at stiffnesses of 0.5 and 1.0. Larger droplets were not seen at a stiffness of 2.0. Camera 1 spread angle decreased slightly as stiffness increased. Camera 2 spread angle remained relatively constant. Some similarity between camera 1 and camera 2 spread angles suggests the spray may be symmetric.

Atomization was not seen in the triplet injector at a stiffness of 0.5. At a stiffness of 1.0, a region of atomization was seen beginning approximately 20 mm from the injector face. At a stiffness of 2.0, atomization was seen beyond approximately 5 mm from the injector face, with intermittent larger droplets. At a stiffness of 0.5, the spray was primarily made up of larger droplets. Some ligaments from primary liquid jet breakup remained. At a stiffness of 1.0, the spray consisted of larger droplets outside the small region of atomization. At a stiffness of 2.0, larger droplets were intermittent throughout the spray. There was no distinct larger droplet region. Camera 1 spread angle increased as stiffness increased, while camera 2 spread angle remained relatively constant. At each stiffness camera 1 spread angle was significantly larger than camera 2 spread angle, suggesting the spray was non-symmetric, and more fan-like in nature.

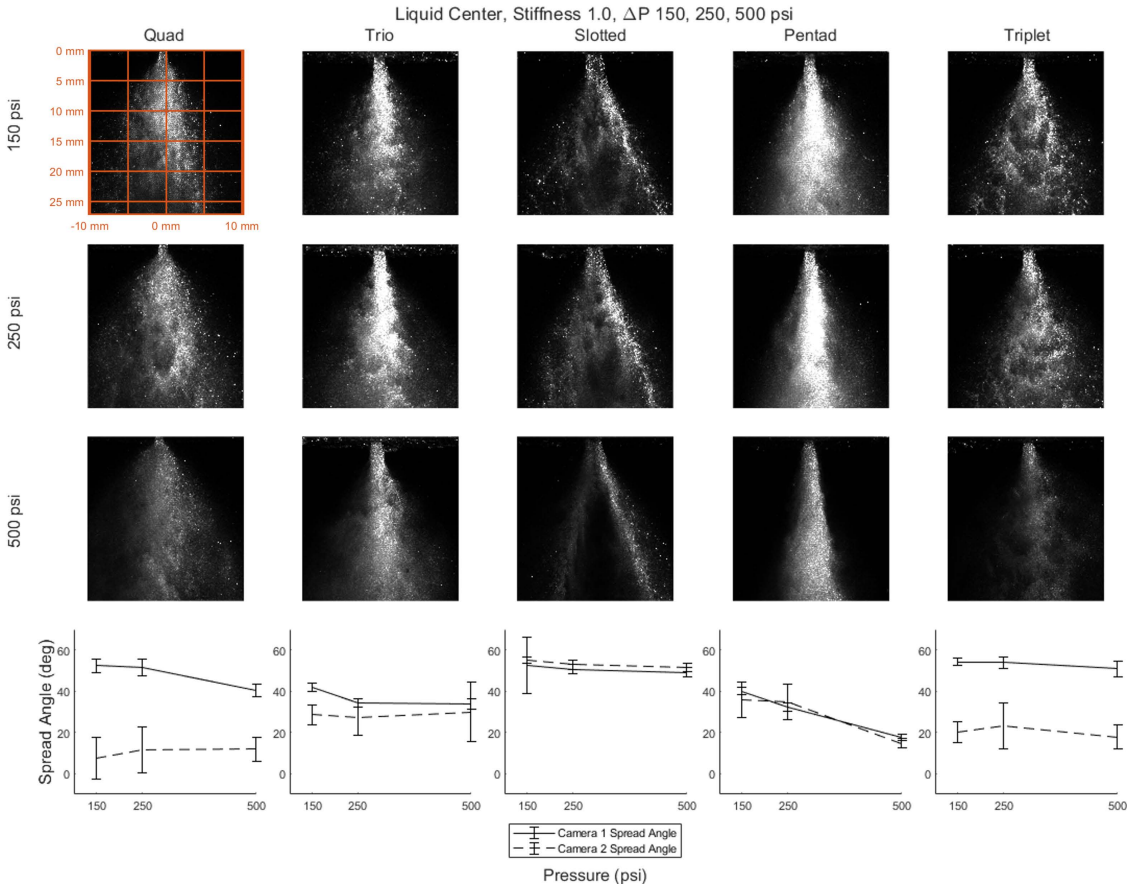

Fig. 8 Instantaneous injector spray images, varying in ΔP, for constant stiffness of 1.0, in liquid centered configuration.

For the quad injector, at ΔP of 150 psi, the atomized region was located primarily in the center-bottom of the spray, beginning approximately 20 mm from the face of the injector. This region of atomization grew upward as ΔP was increased, filling the entire spray at a ΔP of 500 psi. At a ΔP of 150 psi, large droplets were seen at the top and edges of the spray. At a ΔP of 250 psi, large droplets were intermittent throughout the upper and middle spray field. At a ΔP of

500 psi, large droplets were rare, and limited to the outer edges of the spray field. Camera 1 spread angle decreased slightly as ΔP was increased, while camera 2 spread angle increased slightly as ΔP was increased. Camera 2 spread angle was significantly smaller than camera 1 spread angle at each ΔP, suggesting the spray was non-symmetric, and more fan-like in nature.

Analysis of the trio injector is limited due to overexposure seen in the upper region and center of the spray field. Only regions of adequate exposure are considered in this analysis. In all three ΔP cases atomization was seen in the lower region of the spray field. Larger droplets were seen dispersed throughout the spray at a ΔP of 150 psi and were seen with less frequency as ΔP increased. At a ΔP of 500 psi, larger droplets were rare, appearing only in the outer edges of the spray. Camera 1 and camera 2 spread angles trended together as ΔP increased, with camera 1 spread angle slightly less than camera 2. From ΔP of 150 psi to 250 psi, both spread angles decreased slightly. Both spread angles remained constant from ΔP of 250 psi to 500 psi. Camera 1 and camera 2 spread angles were approximately the same at each ΔP, suggesting greater symmetry in the spray field.

For the slotted injector, atomization in the interior of the spray field was seen at ΔP of 150 psi and 250 psi. At ΔP of 500 psi, the interior of the spray field did not contain droplets. In all three ΔP cases large droplets were seen along the boundary of the spray field. Spread angles from both camera views were very similar at every ΔP, decreasing slightly as ΔP increased. Despite this, the lack of droplets found in the center of the spray suggests this spray field was not symmetric.

Analysis of the pentad injector is limited due to overexposure seen in the upper region and center of the spray field. Only regions of adequate exposure are considered in this analysis. Atomization was seen throughout the spray, excluding the overexposed region, in all three ΔP cases. Occasional large droplets were seen in the outer regions of the spray at ΔP of 150 psi and 250 psi. Larger droplets were not seen at a ΔP of 500 psi. Camera 1 and camera 2 spread angles trended together, decreasing significantly as ΔP increased. Strong similarity between camera 1 and camera 2 spread angles suggests the spray may be symmetric.

For the triplet injector, at a ΔP of 150 psi, atomization was limited to the center-bottom of the spray field, beginning approximately 20 mm from the injector face. At a ΔP of 250 psi, atomization was intermittent with larger droplets and limited to the bottom of the spray field, this time beginning 15 mm from the face of the injector. At a ΔP of 500 psi, atomization was seen throughout the spray field. For the ΔP of 150 psi and 250 psi cases, the spray was primarily made up of larger droplets. At a ΔP of 500 psi, larger droplets were infrequent and limited to the outer boundary of the spray. Camera 1 spread angle decreased very slightly as ΔP increased, while camera 2 spread angle increased slightly from ΔP of 150 psi to 250 psi, then decreased slightly from ΔP of 250 psi to 500 psi. At each ΔP, camera 1 spread angle was significantly larger than camera 2 spread angle, suggesting the spray was non-symmetric, and more fan-like in nature.

B. Gas Centered Configuration

The second configuration explored was the gas centered. In this configuration, the outer orifices were plumbed with liquid, and the inner, gas, as shown in Figure 9. Figure 10 shows instantaneous spray images for a range of stiffnesses from camera view 1 while maintaining a constant liquid side ΔP of 250 psi. Figure 11 shows instantaneous spray images for a range of liquid side ΔP from camera view 1 while maintaining a constant stiffness of 1.0. The bottom rows of these figures display spray angle as a function of stiffness and liquid side ΔP, respectively. Spray angle was determined for each image via the process seen in Table 3. In each test, 20 spray image sets were taken at a rate of 2 Hz for a test duration of 10 seconds. The average spray angle and standard deviation were then calculated. Spray angles from both cameras are shown with error bars representing one standard deviation. Every column represents a different injector. Reference scaling is included for visual comparison.

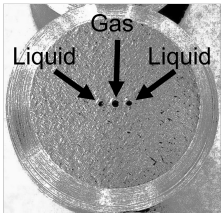

Fig. 9 Orifice identification of a gas centered configuration.

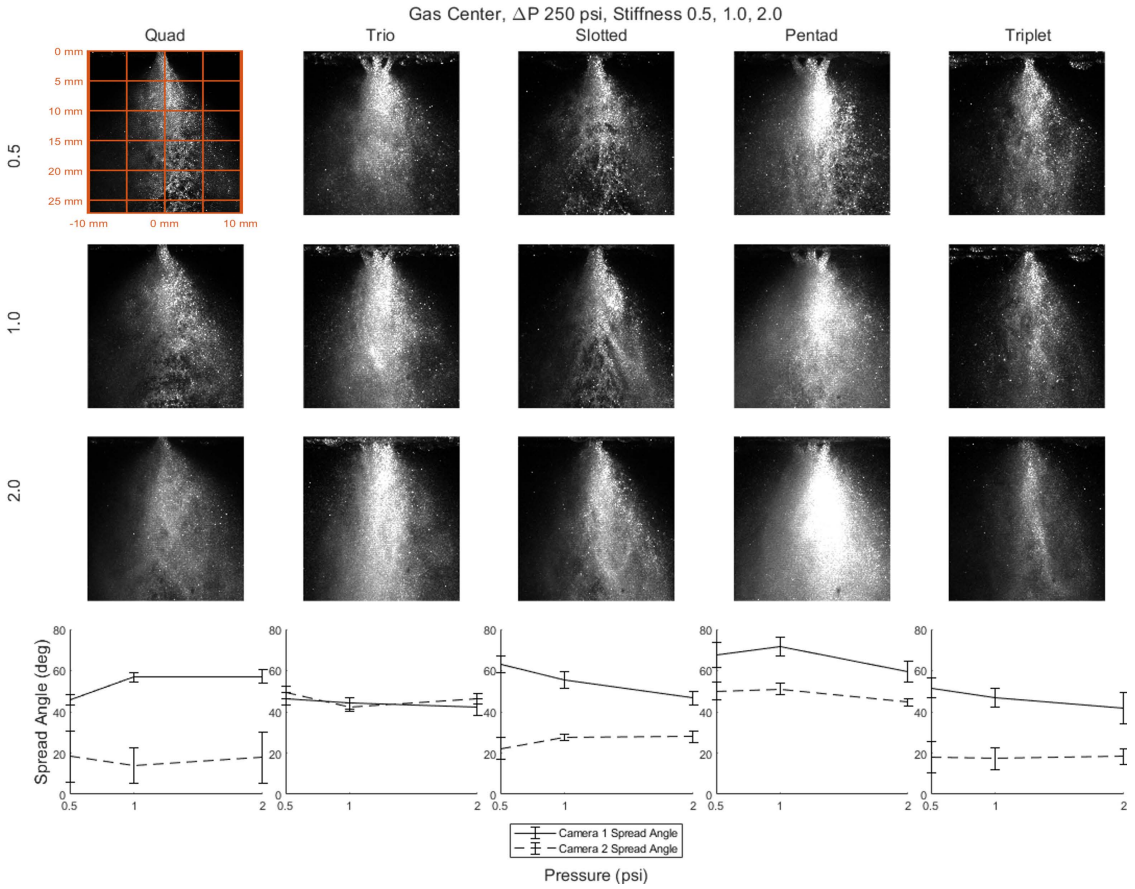

Fig. 10 Instantaneous injector spray images, varying in stiffness, for constant liquid side ΔP of 250 psi, in gas centered configuration.

For the quad injector, the atomized region was located primarily in the outer region of the spray, beginning approximately 5 mm from the face of the injector. The size of this region grew as stiffness was increased. At a stiffness of 2.0, the spray field was fully atomized. For stiffnesses of 0.5 and 1.0, a large droplet region was seen in the center of the spray, approximately 10 mm in width. At a stiffness of 2.0, a few large droplets were seen scattered throughout the spray field. Camera 1 spread angle increased as stiffness was increased from 0.5 to 1.0, and then remained constant from 1.0 to 2.0. Camera 2 spread angle decreased as stiffness was increased from 0.5 to 1.0, and then remained constant from 1.0 to 2.0. Camera 2 spread angle was significantly smaller than camera 1 spread angle at each stiffness, suggesting the spray was non-symmetric, and more fan-like in nature.

Analysis of the trio injector is limited due to overexposure seen in the upper region and center of the spray field. Only regions of adequate exposure are considered in this analysis. Atomization was seen throughout the spray field for all three stiffnesses. Large droplets were dispersed throughout the spray for all three stiffnesses. The frequency of large droplets decreased as stiffness increased, though some remained at a stiffness of 2.0. Camera 1 and camera 2 spread angles remained relatively constant as stiffness was increased and trended together. Camera 1 and camera 2 spread angles were approximately the same at each stiffness, suggesting greater symmetry in the spray field.

For the slotted injector, regions of atomization were seen in the outer areas of the spray at a stiffness of 0.5, beginning approximately 5 mm from the injector face. These regions increased in size, closing inward as stiffness was increased. At a stiffness of 2.0, the entire spray field was atomized. At a stiffness of 0.5, a core region of large droplets approximately 10 mm in width was seen. As stiffness increased, this region closed. At a stiffness of 2.0, occasional droplets were seen toward the outer edges of the spray. Camera 1 spread angle decreased as stiffness increased and camera 2 spread angle increased as stiffness increased. The difference in spread angle between the two views at each stiffness suggests this spray field was not symmetric.

Analysis of the pentad injector is limited due to overexposure seen in the upper region and center of the spray field. Only regions of adequate exposure are considered in this analysis. No clear regions of atomization were seen for a stiffness of 0.5. At stiffnesses of 1.0 and 2.0, atomization was seen in the outer regions of the spray. At a stiffness of 0.5, the core region of the spray consisted primarily of large droplets which were seen with decreasing frequency, moving outward from the center of the spray as stiffness increased. This core region of large droplets was approximately 14 mm wide. At a stiffness of 1.0, the region of large droplets is limited to the center-bottom of the spray, beginning approximately 20 mm from in injector face. Larger droplets were found dispersed throughout the atomized regions of the spray. At a stiffness of 2.0, no regions of large droplets were found. Occasional larger droplets were dispersed throughout the atomized regions of the spray, however less frequent than seen in the stiffness of 1.0 case. Camera 1 and camera 2 spread angles trended together, increasing slightly from stiffnesses of 0.5 to 1.0 and then decreasing from stiffnesses of 1.0 to 2.0. Camera 2 spread angle was less than camera 1 spread angle at each stiffness. The difference between camera 1 and camera 2 spread angles suggests the spray may not have been symmetric.

Atomization was limited in the triplet injector at a stiffnesses of 0.5 and 1.0 and no clear region of atomization devoid of large droplets could be defined. At a stiffness of 2.0, atomization was seen throughout the spray field. At a stiffnesses of 0.5 and 1.0, the spray field was a blend of atomized spray and larger droplets. At a stiffness of 2.0, infrequent larger droplets were found only in the outer edges of the spray. Camera 1 spread angle decreased as stiffness increased, while camera 2 spread angle remained relatively constant. At each stiffness, camera 1 spread angle was significantly larger than camera 2 spread angle, suggesting the spray was non-symmetric, and more fan-like in nature.

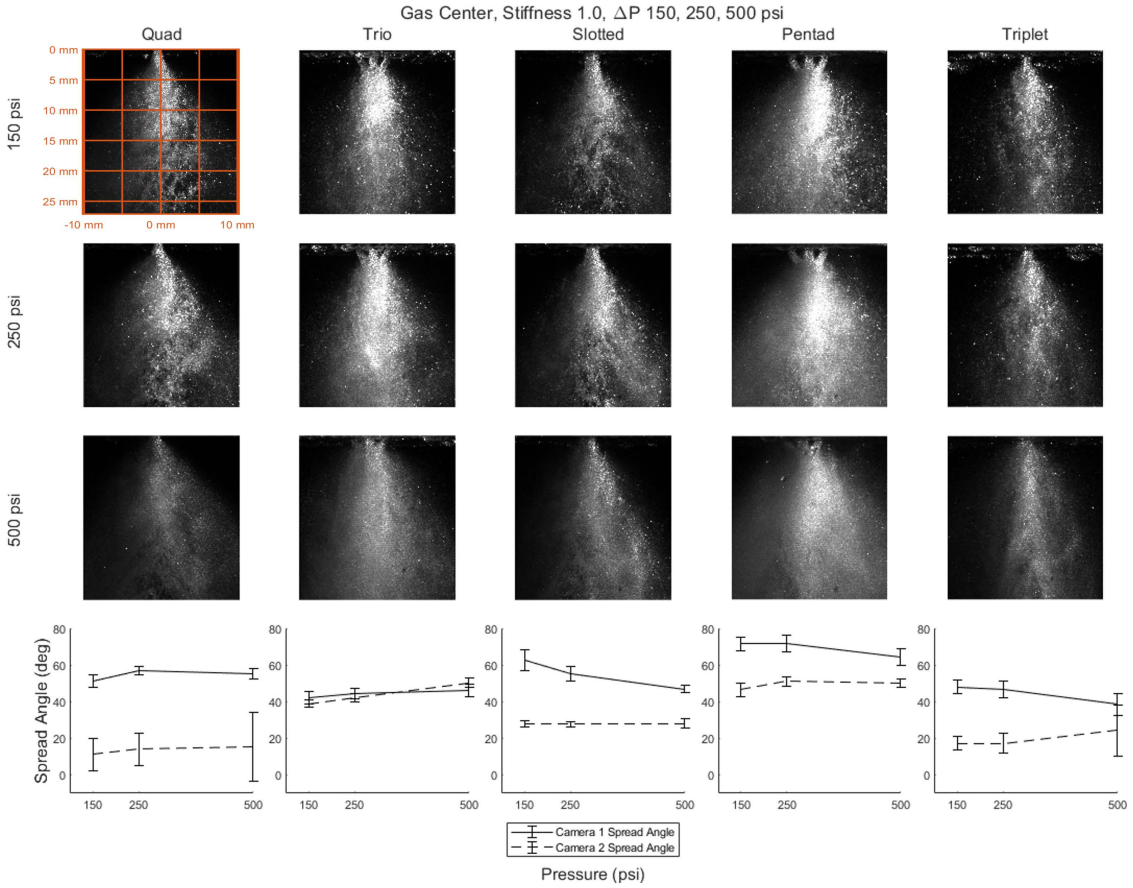

Fig. 11 Instantaneous injector spray images, varying in ΔP, for constant stiffness of 1.0, in gas centered configuration.

For the quad injector, at ΔP of 150 psi, the atomized region was located primarily in the upper and outer regions of the spray. This region of atomization grew downward and inward as ΔP was increased. At a ΔP of 500 psi, the spray was atomized everywhere except a small triangular region starting 20 mm from the injector face. At ΔP of 150 psi and

250 psi, large droplets were found in the center of the spray, starting around 15 mm from the injector face. At a ΔP of 500 psi, large droplets were limited to the small triangular region previously mentioned. Camera 1 and camera 2 spread angles trended together, increasing slightly as ΔP was increased from 150 psi to 250 psi, and then remaining constant from 250 psi to 500 psi. Camera 2 spread angle was significantly smaller than camera 1 spread angle at each ΔP, suggesting the spray was non-symmetric, and more fan-like in nature.

Analysis of the trio injector is limited due to overexposure seen in the upper region and center of the spray field. Only regions of adequate exposure are considered in this analysis. In all three ΔP cases atomization was seen throughout the spray field. Larger droplets were seen dispersed throughout the spray at a ΔP of 150 psi and were seen with less frequency as ΔP increased. At a ΔP of 500 psi larger droplets were rare, appearing dispersed throughout the spray. Camera 1 and camera 2 spread angles trended together, slightly increasing as ΔP increased. Camera 1 and camera 2 spread angles were approximately the same at each ΔP, suggesting greater symmetry in the spray field.

For the slotted injector, atomization was limited to the outer boundary of the spray at a ΔP of 150 psi. These regions of atomization grew inward and downward as ΔP was increased. At a ΔP of 500 psi, the spray was atomized everywhere, except for a small triangular region starting 20 mm from the injector face. In all three ΔP cases a core large droplet region was seen in the lower portion of the spray, internal to the regions of atomization. Camera 1 spread angle decreased as ΔP increased. Camera 2 spread angle remained constant as ΔP increased. For all ΔP cases, camera 2 spread angle was significantly less than camera 1 spread angle, suggesting this spray field was not symmetric.

Analysis of the pentad injector is limited due to overexposure seen in the upper region and center of the spray field. Only regions of adequate exposure are considered in this analysis. Atomization was seen throughout the spray, excluding the overexposed region, in all three ΔP cases. Many large droplets were seen mixed throughout the atomized spray at a ΔP of 150 psi. At a ΔP 250 psi, the large droplets were primarily limited to the lower central portion of the spray approximately 20 mm off the injector face, however more dispersed large droplets were seen around the edges of the spray. Few larger droplets were seen near the edges of the spray at a ΔP of 500 psi. Camera 1 spread angle was constant as ΔP increased from ΔP of 150 psi to 250 psi and then decreased from 250 psi to 500 psi. Camera 2 spread angle increased as ΔP increased from ΔP of 150 psi to 250 psi and then remained constant from 250 psi to 500 psi. Camera 2 spread angle was less than camera 1 spread angle in each ΔP case. The difference between camera 1 and camera 2 spread angles suggests the spray may not have been symmetric.

For the triplet injector, at a ΔP of 150 psi, atomization was limited to the center-bottom of the spray field, beginning approximately 20 mm from the injector face. At a ΔP of 250 psi, atomization was intermittent with larger droplets and limited to the bottom of the spray field, beginning 15 mm from the face of the injector. At a ΔP of 500 psi, atomization was seen throughout the spray field. At a ΔP of 150 psi, the spray was primarily made up of larger droplets. At a ΔP of 250 psi, larger droplets were limited to the upper region of the spray. At a ΔP of 500 psi, larger droplets were infrequent and limited to the outer boundary of the spray. Camera 1 spread angle decreased very slightly as ΔP increased, while camera 2 spread angle increased slightly from as ΔP increased. At each ΔP, camera 1 spread angle was significantly larger than camera 2 spread angle, suggesting the spray was non-symmetric, and more fan-like in nature.

V. Conclusions

A high-pressure, cold flow, single element injector testing facility was developed to better understand the spray structure of additively manufactured injector elements. Quad, trio, pentad, slotted, and triplet impingers in gas-liquid flow were analyzed. These injectors were orthogonally photographed simultaneously while using a high energy pulsed laser. The injectors were tested in GLG and LGL configurations in iterations of stiffnesses of 0.5, 1.0 and 2.0 and differential liquid side pressures of 150, 250 and 500 psi. In each of these iterations, 20 images were taken at a rate of 2Hz for both camera angles. Each of these images were processed for spread angles and reviewed for visual indications of atomization. The results of this work are shown above.

Preliminary results suggest the pentad injector has the highest levels of atomization across a broad range of ΔP and stiffness conditions. Results also show the trio spread angle is the least susceptible to variations in ΔP and stiffness condition. Pentad was found to produce the most symmetric spray for liquid centered configuration and trio was found to produce the most symmetric spray for gas centered configurations.

Facility improvements are planned for future work including a more robust illumination system, the introduction of stereophotogrammetry, and the introduction of a lidar system. The addition of a beam splitter for cross-illumination is predicted to eliminate overexposure. Future cold flow investigations will focus on a broader range of injector spray characteristics. Additional future work is underway in the development of a single injector element hotfire testing facility.

Acknowledgments

The authors would like to acknowledge NASA Marshall for funding this work under CAN 0972-21P/EN21041, Alabama Space Grant Consortium for fellowship funding under NASA Training Grant NNH19ZHA001C, the members of Auburn University's Advanced Flow Diagnostics Lab for use of their dual-pulse Nd:YAG New Wave Solo III laser and programmable timing unit, and Ph.D. Candidate Daniel Stubbs for his support.

References

[1] Blakey-Milner, B., Gradl, P., Snedden, G., Brooks, M., Pitot, J., Lopez, E., Leary, M., Berto, F., and du Plessis, A., "Metal additive manufacturing in aerospace: A review," *Materials and Design*, Vol. 209, 2021, p. 110008. https://doi.org/https://doi.org/10.1016/j.matdes.2021.110008, URL https://www.sciencedirect.com/science/article/pii/S0264127521005633.

[2] Busachi, A., Erkoyuncu, J., Colegrove, P., Martina, F., Watts, C., and Drake, R., "A review of Additive Manufacturing technology and Cost Estimation techniques for the defence sector," *CIRP Journal of Manufacturing Science and Technology*, Vol. 19, 2017, pp. 117–128. https://doi.org/https://doi.org/10.1016/j.cirpj.2017.07.001, URL https://www.sciencedirect.com/science/article/pii/S1755581717300299.

[3] Pradel, P., Zhu, Z., Bibb, R., and Moultrie, J., "Complexity is not for free: the impact of component complexity on additive manufacturing build time," *Rapid Design, Prototyping and Manufacturing*, 2017.

[4] Kerstens, F., Cervone, A., and Gradl, P., "End to end process evaluation for additively manufactured liquid rocket engine thrust chambers," *Acta Astronautica*, Vol. 182, 2021, pp. 454–465. https://doi.org/https://doi.org/10.1016/j.actaastro.2021.02.034, URL https://www.sciencedirect.com/science/article/pii/S0094576521001089.

[5] Schwer, D., Corrigan, A., Taylor, B., and Kailasanath, K., "On reducing feedback pressure in rotating detonation engines," *51st AIAA Aerospace Sciences Meeting including the New Horizons Forum and Aerospace Exposition*, 2013, p. 1178.

[6] Teasley, T., Williams, B., Gradl, P., and Protz, C., "PERFORMANCE VARIABILITY OF ADDITIVELY MANUFACTURED LIQUID ROCKET INJECTORS WITH POST-PROCESSING TECHNIQUES," *68th JANNAF Propuls. Meet.*, 2021.

[7] Lim, D., Heister, S., Stechmann, D., and Kan, B., "Transient response of a liquid injector to a steep-fronted transverse pressure wave," *Shock Waves*, Vol. 28, No. 4, 2018, pp. 919–932. https://doi.org/10.1007/s00193-017-0787-8, URL https://doi.org/10.1007/s00193-017-0787-8.

[8] Lefebvre, A. H., *Atomization and Sprays*, 1988.

[9] Song, W., and Koo, J., "Spray patterns of multi-element swirl coaxial injector of interacting spray under different injection conditions," *AIP Advances*, Vol. 11, No. 7, 2021, p. 075030. https://doi.org/10.1063/5.0058107, URL https://aip.scitation.org/doi/abs/10.1063/5.0058107.

[10] Kenny, R., Moser, M., Hulka, J., and Jones, G., "Cold flow testing for liquid propellant rocket injector scaling and throttling," *42nd AIAA/ASME/SAE/ASEE Joint Propulsion Conference and Exhibit*, 2016, p. 4705.

[11] Cenik, B., Suer, T. U., and Uslu, S., "ATOMIZATION AND COMBUSTION CHARACTERISTICS OF IMPINGING INJECTORS IN LIQUID ROCKET ENGINES," 2019.

[12] Wei, X., Feng, Y., Ye, J., Li, N., and Haidn, O. J., "Influence of Mass Flow Rate on the Atomization Characteristics of Screw Conveyor Swirl Injectors," *Aerospace*, Vol. 9, No. 6, 2022, p. 293. URL https://www.mdpi.com/2226-4310/9/6/293.

[13] Zhou, W., Xu, X., Yang, Q., Zhao, R., and Jin, Y., "Experimental and numerical investigations on the spray characteristics of liquid-gas pintle injector," *Aerospace Science and Technology*, Vol. 121, 2022, p. 107354.

[14] Teasley, T. W., Protz, C. S., Larkey, A. P., Williams, B. B., and Gradl, P. R., "A Review Towards the Design Optimization of High Performance Additively Manufactured Rotating Detonation Rocket Engine Injectors," , 2021. https://doi.org/10.2514/6.2021-3655, URL https://arc.aiaa.org/doi/abs/10.2514/6.2021-3655.

[15] Burick, R. J., "Atomization and mixing characteristics of gas/liquid coaxial injector elements," *AIAA Journal*, , No. 14, 1972, p. 2291.

[16] Bigler, B. R., Paulson, E. J., and Hargus, W. A., "Idealized efficiency calculations for rotating detonation engine rocket applications," *53rd AIAA/SAE/ASEE Joint Propulsion Conference*, 2017, p. 5011.

[17] Anderson, W. S., Heister, S. D., Kan, B., and Hartsfield, C., "Experimental Study of a Hypergolically Ignited Liquid Bipropellant Rotating Detonation Rocket Engine," *Journal of Propulsion and Power*, Vol. 36, No. 6, 2020, pp. 851–861. https://doi.org/10.2514/1.B37666, URL https://doi.org/10.2514/1.B37666, doi: 10.2514/1.B37666.

[18] Gaillard, T., Davidenko, D., and Dupoirieux, F., "Numerical simulation of a rotating detonation with a realistic injector designed for separate supply of gaseous hydrogen and oxygen," *Acta Astronautica*, Vol. 141, 2017, pp. 64–78.

[19] Prakash, S., Raman, V., Lietz, C. F., Hargus Jr, W. A., and Schumaker, S. A., "Numerical simulation of a methane-oxygen rotating detonation rocket engine," *Proceedings of the Combustion Institute*, Vol. 38, No. 3, 2021, pp. 3777–3786.

[20] Wu, K.-J., Su, C.-C., Steinberger, R., Santavicca, D., and Bracco, F., "Measurements of the spray angle of atomizing jets," 1983.

[21] Reitz, R. D., and Bracco, F., "On the dependence of spray angle and other spray parameters on nozzle design and operating conditions," Report 0148-7191, SAE technical paper, 1979.

[22] De Corso, S. M., and Kemeny, G. A., "Effect of Ambient and Fuel Pressure on Nozzle Spray Angle," *Transactions of the American Society of Mechanical Engineers*, Vol. 79, No. 3, 2022, pp. 607–614. https://doi.org/10.1115/1.4013107, URL https://doi.org/10.1115/1.4013107.

[23] ASABE, S., "S572,"Spray Nozzle Classification by Droplet Spectra," American Society of Agricultural and Biological Engineers, St," *Joseph, MI*, 1999.

[24] Otsu, N., "A Threshold Selection Method from Gray-Level Histograms," *IEEE Transactions on Systems, Man, and Cybernetics*, Vol. 9, No. 1, 1979, pp. 62–66. https://doi.org/10.1109/TSMC.1979.4310076.

[25] Soille, P., *Morphological image analysis: principles and applications*, Vol. 2, Springer, 1999.